Neutron adiabaticity and its impact on data analysis, illustrated for polarized GISANS

Annika Stellhorn^{1*}, Wai-Tung Lee², Emmanuel Kentzinger³, Wangchun Chen⁴, Jonathan Gaudet^{4,5}, Kathryn Krycka⁴ and Elizabeth Blackburn¹

Abstract. The significance of neutron spin adiabaticity in the data analysis of polarized Grazing Incidence Small Angle Neutron Scattering (GISANS) is discussed, with the aim of minimizing the number of simulation parameters of complex magnetic models within the neutron scattering cross-section. We illustrate how an estimate of the neutron polarization direction and adiabaticity can be obtained by magnetic field and neutron ray-tracing simulations and compare the results with measurements of the magnetic field map for the beamline used in the GISANS experiment. We show how small deviations from the neutron polarization direction with respect to the magnetic field vector at the sample position significantly affect the data analysis, and how this can be considered within the magnetic model of the scattering cross section using the Distorted Wave Born Approximation.

1 Introduction and science case

In neutron scattering, the adiabaticity of neutron spin transport, A, quantifies how well the semi-classical neutron polarization vector in the density matrix formalism, \vec{P} , follows the direction of magnetic field, \vec{B} . In polarized neutron scattering, maintaining a high neutron spin-transport adiabaticity along the beam path between spin-conditioning and detection components, such as polarizer, analyzer, and spin-flippers, and the sample is crucial. If the adiabaticity drops too low in a particular region on the beam path, this can severely affect the quality of the results obtained from neutron experiments with polarization analysis. To deal with these cases of critically low adiabaticity, precise simulations of the neutron polarization evolution along the flight path are needed to evaluate the polarization at the sample position, which is then put into the simulations of the scattering pattern generated by the sample. In this article, we demonstrate the determination of the neutron adiabaticity and polarization by a combination of magnetic field modelling and neutron ray-tracing, and the effect of an imperfect neutron transport on the data analysis, using the example of polarized GISANS from the magnetic domains and domain walls in a thin film of FePd.

The adiabaticity is defined as the ratio of the Larmor frequency of the neutron spin, ω_L , and the angular frequency of the magnetic field along the neutron flight path, ω_B :

$$A = \frac{\omega_L}{\omega_B} = \frac{\gamma |\vec{B}|}{\left| \nabla \left(\frac{\vec{B}}{|\vec{B}|} \right) \cdot \overrightarrow{v_n} \right|} \tag{1}$$

where γ is the gyromagnetic ratio of the neutron, $\overrightarrow{B}(x,y,z)$, is the magnetic field vector, and $\overrightarrow{v_n}$ is the velocity of the neutrons. The gradient term is the Jacobian of the magnetic field direction vector. Multiplying the Jacobian with $\overrightarrow{v_n}$ gives the vector of the rate of change of the field direction vector along $\overrightarrow{v_n}$. It is a measure of the ability of the neutron polarization to follow the magnetic field as the field direction changes.

Two aspects have to be considered: (i) the Larmor precession of the neutron spin, i.e. the evolution of the components of \vec{P} perpendicular to the magnetic field, and (ii) the component of \vec{P} along the magnetic field \vec{B} . The evolution of the angle between \overrightarrow{P} and \overrightarrow{B} is of importance for the neutron adiabaticity. The adiabaticity is a measurement of part (ii). The evolution of \vec{P} along the neutron flight path can be determined by a combination of 3D magnetic field simulations together with neutron ray-tracing programs, with the simulations verified by measurements of the magnetic field profile of the setup. Our experiment belongs to a class of polarized neutron experiments known as uniaxial polarization analysis [1], which measures the component of neutron polarization along \vec{B} . This means that it does not measure the components of \vec{P} perpendicular to the magnetic field, and so the effects of

¹Lund University, Division of Synchrotron Radiation Research, 22100 Lund, Sweden

²European Spallation Source (ESS), Instrument Technologies Division, 22484 Lund, Sweden

³Forschungszentrum Jülich GmbH, Jülich Centre for Neutron Science (JCNS-2) and Peter Grünberg Institut (PGI-4), JARA-FIT, 52428 Juelich, Germany

⁴NIST Center for Neutron Research, National Institute of Standards and Technology, Gaithersburg, Maryland 20899, USA

⁵Department of Materials Science and Eng., University of Maryland, College Park, MD 20742-2115

^{*} Corresponding author: annika.stellhorn@sljus.lu.se

Larmor precession are not measured. The change of the component of \vec{P} along \vec{B} by the sample is one of the main focuses of uniaxial polarization analysis. Other techniques do measure the component of \vec{P} perpendicular to \vec{B} , such as spherical polarimetry techniques using CRYOPAD [2] or MuPAD [3], or methods like spin-echo SANS [4].

To model the neutron scattering cross-section from polarized GISANS experiments, we use the Distorted Wave Born Approximation (DWBA) extended by the paracrystal theory, and with an appropriate model for the domain and domain wall pattern [5-7], which describes the lateral correlations probed by GISANS. This model of the domain wall pattern includes a number of sample-specific parameters (e.g. domain and domain wall width, the in-plane distribution and correlation length of the domain structure, and closure domain sizes). In addition, if the neutron polarization does deviate from pointing along the magnetic field axis during spin-transport between the polarizer and the sample, and between the sample and the analyzer, this will affect the result, introducing additional parameters into the simulation.

Together, the combination of magnetic field modelling, analysis of the neutron polarization by ray tracing, and simulations of the scattering cross-section, allow us to minimize the simulation parameters needed for the analysis of polarized GISANS experiments on complex magnetic structures. In this paper, we provide a detailed example of this approach, illustrating how important it is when interpreting experimental results. First, we outline the necessary information about the specific sample, and show some polarized GISANS data collected from it. We demonstrate how the magnetic field simulations combined with neutron ray-tracing can be used for data analysis on the magnetic domain structure by the DWBA. Finally, we discuss the effect of an imperfect neutron spin transport on the analysis of the magnetic domain structure by the DWBA.

2 Polarized GISANS on high-PMA FePd heterostructures

2.1 Magnetic domains and domain walls

L10-ordered FePd thin films with a high structural ordering of the Fe and Pd atoms give rise to a high perpendicular magnetic anisotropy (PMA), described by the uniaxial magnetocrystalline anisotropy constant K_u . In films with the crystalline c axis parallel to the surface normal, this leads to the formation of two set of domains with their magnetization respectively parallel or antiparallel to the film normal [8]. The specific forms of domains observed depends strongly on the way the film is grown, and the strength of the magneto-crystalline anisotropy energy $E_{\rm ma}$ and shape anisotropy energy $E_{\rm sh}$ can be effectively controlled [9-11]. These terms then determine the domain width, the domain wall width, the size of any closure domains, and the stray field strength associated with the magnetic domains. For materials like these FePd films, the ratio of the magnetocrystalline

anisotropy constant K_u and the shape anisotropy constant K_{sh} is a measure of the strength of the PMA:

$$K = \frac{K_u}{K_{Sh}} \tag{2}$$

If K > 1, high PMA is achieved. Further details are given in Refs. 8 and 9. For our purposes here, the sample in question develops a maze-like structure (Fig. 1(a)) and consists of no or very small expected closure domains due to the very high PMA ($K = 2 \pm 0.1$). Following Ref. [12], Bloch domain walls form between the out-of-plane oriented magnetic domains (Fig. 1(b)). The K-value, saturation magnetization, coercive field, measured domain periods, as well as theoretical domain and domain wall sizes for the relevant sample are listed in Table 1.

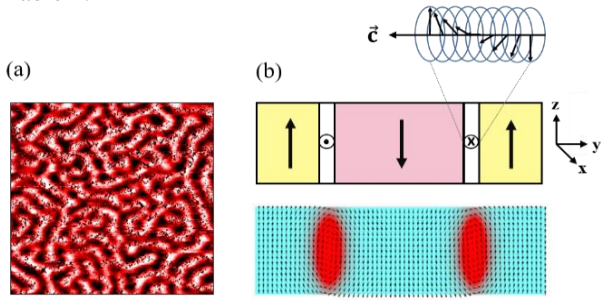


Fig. 1: (a) $3x3\mu m$ Magnetic Force Microscopy measurements on the domain pattern for a PMA FePd thin film with $K=2\pm0.1$ at room temperature. (b) (top) sketch of the side-view of the magnetic domains in the out-of-plane direction (yellow and red) and the Bloch domain walls (white) containing a net chirality with chiral propagation along \vec{C} . (bottom) A visualization on the magnetic vector orientation by micromagnetic simulations on high-PMA FePd with K=1.5 by van der Laan *et al.* [13].

Table 1. Magnetic properties of the investigated high-PMA FePd thin film [10]. The theoretical domain wall size is calculated based on the exchange constant $A_{ex} = 10^{-11}$ J/m [14].

<i>K</i> -value	2 ± 0.1
Saturation	$(1.09 \pm 0.05) \ 10^6 \ A/m$
magnetization	
Coercive field	$H_{c,\perp} = (6 \pm 2) \text{ mT}; H_{c,\parallel} = (31 \pm 1)$
	mT
Measured domain	$(110 \pm 5) \text{ nm}$
width	
Theoretical domain	≈ 8 nm
wall size	

The sketch in Fig. 1(b) assumes chiral Bloch walls with a preferred orientation of chirality \vec{c} parallel to the thin film surface (i.e., in the *x-y*-plane). Considering the centrosymmetric L1₀-structural phase of FePd without inversion asymmetry, no bulk-like Dzyaloshinskii–Moriya interaction (DMI) is favored in the thick FePd film investigated in this study ($d_{FePd} = 44 \pm 5$ nm). Additionally, the domain width $w_D = 110 \pm 5$ nm is large in comparison to the Bloch domain wall width $w_{DW} \approx 8$ nm (see Table 1) and so the magnetic exchange length in FePd does not support a magnetic interaction between neighboring domain walls. In summary, the formation

of a net chirality from Bloch domain walls is not

However, the actual sample is a heterostructure stack of Pd (cap, 1nm) / Nb (39nm) / FePd(44nm) / Pd (buffer, 60nm) / Cr (seed, 1nm) / MgO (substrate), where symmetry breaking at the interface of the FePd and the heavy metal buffer layer Pd may lead to interlayer DMI [15]. In multilayer structures composed of ultrathin films, this has been shown to lead to chiral Néel walls [15], but Pollard et al. [16] have shown that a combination of the interfacial symmetry breaking and the demagnetization field resulting from dipole-dipole interactions can favor the formation of chiral Bloch walls. In this experiment, we have observed asymmetric GISANS peaks in the spin flip (SF) channel that are generated by scattering from the Bloch domain walls. As will be explained in the following sections, nuclearmagnetic interactions can be ruled out as the origin of the SF asymmetry and hence it can be explained only by the existence of chiral domain walls. To be sensitive to such chiral structures, the neutron polarization direction \overrightarrow{P} must have components parallel to the propagation direction of the chirality \vec{c} , which for Bloch domain walls lies within the surface plane (Fig. 1b). In our experiment, the expected neutron polarization is parallel to the external magnetic field applied perpendicular to the sample surface. This motivated a detailed investigation of the magnetic field vector at the sample position and the neutron adiabaticity along the beam path.

2.2 Polarized GISANS

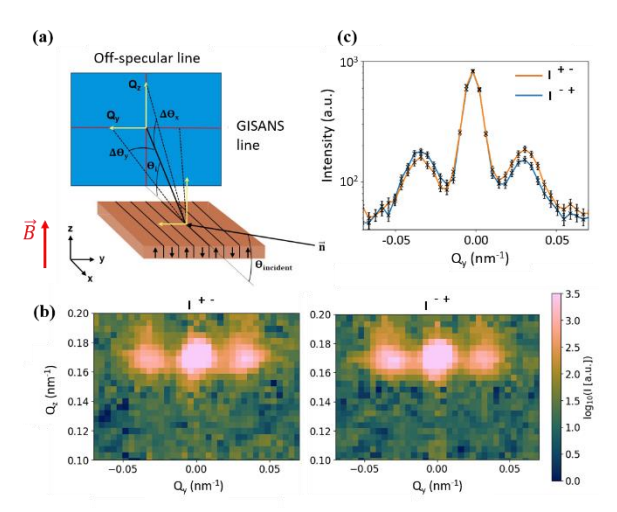


Fig. 2. (a) The scattering geometry of the polarized GISANS measurements that probe $I(Q_y,Q_z)$. The specular and GISANS lines are shown on the detector in red; the magnetic field is applied along the z-axis. (b) Measured SF intensity maps in the Q_y - Q_z plane for the channels I^{+-} (left) and I^{-+} (right) at $T = (10.10 \pm 0.02)$ K. The line at $Q_z = 0.17$ nm⁻¹ corresponds to the GISANS line, n denotes the incident neutron beam. (c) $I(Q_y)$ integrated over 0.137 nm⁻¹ < Q_z < 0.2 nm⁻¹ for the data in panel (b).

In combination with polarization analysis, GISANS can provide insight into both in- and out-of-plane oriented chiral magnetic domain walls, and is therefore a logical choice for studying domain structures of the type that can be engineered into FePd thin films [11]. The neutron beam comes in with an angle close to the critical angle for total external reflection, θ_c . Using the small-angle approximation, the scattering vector \vec{Q} is described by Eq. 3 [17], with the incident- and reflected angles θ_i and θ_f , as well as the off-specular scattered angles $\Delta\theta_x$ and $\Delta\theta_y$ (see Fig. 2(a)). The Q_y -line at $\theta_i = \theta_f$ is called the GISANS-line.

$$\begin{pmatrix} Q_{x} \\ Q_{y} \\ Q_{z} \end{pmatrix} = \frac{2\pi}{\lambda} \begin{pmatrix} \theta_{i} \Delta \theta_{x} + \frac{(\Delta \theta_{x})^{2}}{2} + \frac{(\Delta \theta_{y})^{2}}{2} \\ \Delta \theta_{y} \\ 2\theta_{i} + \Delta \theta_{x} \end{pmatrix}$$
(3)

Fig. 2(b) shows the SF channels of a polarized GISANS measurement on our high-PMA FePd thin film at T = 10 K and θ_i close to θ_c , measured at the vSANS beamline at NIST [18,19], with Q_z -integrated $I(Q_y)$ linecuts integrated over the range 0.137 nm⁻¹ $< Q_z < 0.2$ nm⁻¹ shown in Fig. 2(c). The experiment was carried out with a sample-to-detector distance of 15 m and a neutron wavelength of 8 Å with a wavelength spread of 12 %. A guide field perpendicular to the thin film surface of $B_{\perp} = 2.6$ mT was applied. This configuration gives rise to GISANS peaks in the SF channels $Q_y = \pm 0.033$ nm¹, corresponding to a period of 96 nm. The peaks were generated by scattering from the Bloch domain walls which have a magnetic induction perpendicular to the applied field direction. A specular peak arising due to inefficiencies in the polarizer, spintransport, spin flipper, and the analyzer. If the polarization components and spin-transport in between are perfect, there should be no specular peak at this position. The whole-system setup without the sample has a flipping ratio of 45, with the analyser efficiency previously measured to be $P_{an} = 0.988$.

The measurements show a clear asymmetry between the left and right GISANS peak (Fig. 2(c)). This arises due to the non-zero average chirality of the Bloch domain walls in the sample, which we now illustrate.

The total elastic scattering cross section for the interaction of a neutron beam with a magnetic sample is:

$$\sigma = \sigma_N + \sigma_M + \sigma_{NM} + \sigma_{M \times M} \tag{4}$$

where σ_N is the nuclear scattering contribution, σ_M is the magnetic scattering from non-chiral magnetic structure, σ_{NM} is the nuclear-magnetic interference term, and $\sigma_{M\times M}$ is an additional contribution that is only non-zero for chiral magnetic arrangements [20-22]. To describe the scattering patterns obtained from polarized measurements, the incident and final neutron polarizations need to be taken into account, such that the total elastic scattering cross section is

$$\begin{split} \overrightarrow{P'}I &= \overrightarrow{P} \left(\widetilde{N} N - \frac{1}{3} I_{si} \right) + \left(\overrightarrow{P} \cdot \overrightarrow{M}_{\perp} \right) \overrightarrow{M}_{\perp} + \\ \left(\overrightarrow{P} \cdot \overrightarrow{M}_{\perp} \right) \overrightarrow{M}_{\perp} - \overrightarrow{P} \left(\overrightarrow{M}_{\perp} \cdot \overrightarrow{M}_{\perp} \right) + i N \left(\overrightarrow{P} \times \overrightarrow{M}_{\perp} \right) - \\ i \widetilde{N} \left(\overrightarrow{P} \times \overrightarrow{M}_{\perp} \right) + N \overrightarrow{M}_{\perp} + \widetilde{N} \overrightarrow{M}_{\perp} - i \left(\overrightarrow{\widetilde{M}}_{\perp} \times \overrightarrow{M}_{\perp} \right) \end{split} \tag{5}$$

where $\overrightarrow{P'}$ is the outgoing polarization of the beam, \overrightarrow{P} is the ingoing polarization, N is Fourier transform of the

nuclear structure factor, with its complex conjugate \widetilde{N} , $\overrightarrow{M}_{\perp}$ is the Fourier transform of the sample magnetization component perpendicular to the scattering vector \overrightarrow{Q} , with complex conjugate \widetilde{M}_{\perp} , and I_{si} the nuclear spin-incoherent scattering intensity. This shows that only magnetization components perpendicular to \overrightarrow{Q} are

From Eq. 5, for a specific polarization direction ν in any Cartesian direction, the asymmetric scattering contributions to σ are [22]:

$$\Delta^{SF}_{\nu} \approx 2i \left(\overrightarrow{\tilde{M}}_{\perp} \times \overrightarrow{M}_{\perp} \right)_{\nu} \tag{6}$$

$$\Delta^{NSF}_{\nu} \approx 2\Re\left(N\overrightarrow{\widetilde{M}}_{\perp,\nu}\right)^{\nu} \tag{7}$$

for the SF and non-spin-flip (NSF) channels respectively. A contribution from any chirality with propagation vector $\vec{\boldsymbol{C}}$ parallel to $(\vec{\boldsymbol{M}}_{\perp} \times \vec{\boldsymbol{M}}_{\perp})_{\nu}$ in the direction of the neutron polarization will therefore lead to asymmetric scattering peaks in the SF channels.

For our polarized GISANS measurements, we have used a setup with guide field direction perpendicular to the thin film surface and hence perpendicular to $\vec{\boldsymbol{C}}$ of Bloch domain walls in high-PMA FePd as shown in Fig. 1. From Eq. 6, only components of $\vec{\boldsymbol{C}}$ parallel to $\vec{\boldsymbol{P}}$ will lead to asymmetric spin-flip GISANS peaks. The observed asymmetry in Fig. 2(c) could therefore arise due to a misalignment between $\vec{\boldsymbol{P}}$ and the sample surface normal.

In Section 3, we discuss how the polarization direction may be affected by adiabaticity during spin-transport along the neutron flight path. First, however, we describe the magnetic model used to calculate the total scattering cross section, based on previous models developed by Toperverg and Kentzinger [5,6].

2.3 Description of the DWBA simulation of polarized GISANS measurements on high-PMA FePd

Within the Distorted Wave Born Approximation (DWBA), the neutron scattering cross section $d\sigma/d\Omega$ from a GISANS experiment can be calculated assuming a depth-dependent, laterally homogeneous magnetic potential $\hat{V}_{0,l}(z)$ inside each layer l, which is perturbed by a lateral inhomogeneous magnetic potential $\hat{V}_{pert,l}(\vec{s})$, where \vec{s} is a 2D vector within the plane of the sample surface (Fig. 3).

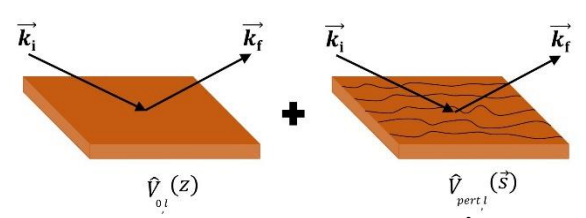


Fig. 3. Non-perturbed scattering potential $\hat{V}_{0,l}(z)$ of a homogeneous sample and perturbation potential $\hat{V}_{pert,l}(\vec{s})$ of a sample with lateral inhomogeneous structural or magnetic density [10].

This leads to off-specular scattering:

$$\frac{d\sigma}{d\Omega} \left(\theta_{l}, \theta_{f}, \overrightarrow{\boldsymbol{Q}}_{//} \right) = |\frac{m_{n}}{2\pi\hbar^{2}} \sum_{l} \left\langle \psi_{f,l} \left| \widehat{V}_{pert,l}(\overrightarrow{\boldsymbol{s}}) \middle| \psi_{i,l} \right. \right\rangle |^{2} \quad (8)$$

with $\psi_{f,l}$ being the distorted wavefunction inside layer l after the scattering event, $\psi_{i,l}$ the distorted wavefunction inside l just before the scattering event, and $\overrightarrow{Q}_{//}$ the inplane component of the scattering wave vector. Further details are given in Ref. [6].

The perturbation potential $\hat{V}_{pert,l}(\vec{s})$ is given by the sum of the nuclear and magnetic scattering length density fluctuations $\tilde{\rho}_{N,l}(\vec{s})$ and $\tilde{\rho}_{M,l}(\vec{s})$ respectively:

$$\hat{V}_{pert,l}(\vec{\boldsymbol{s}}) = \frac{2\pi\hbar^2}{m_n} (\tilde{\rho}_{N,l}(\vec{\boldsymbol{s}}) \cdot \hat{1} + \tilde{\rho}_{M,l}(\vec{\boldsymbol{s}}) \vec{\boldsymbol{\sigma}} \cdot \vec{\boldsymbol{b}}_l) \quad {}_{(9)}$$

where $\vec{\hat{\sigma}}$ is the vector of Pauli matrices and \vec{b}_l is the unit vector parallel to the magnetic field in layer l. Theoretical descriptions of $\tilde{\rho}_{M,l}(\vec{s})$ of the magnetic domain structure of a high-PMA material, like FePd, using the DWBA have been formulated by Toperverg and Kentzinger [5,6]. In a material with a maze domain structure, this model has to be extended by the paracrystal theory [7] and integration over the in-plane oriented domain orientations. The maze domain pattern has to be divided into subunits of an ordered subsystem, each consisting of two antiparallel out-of-plane oriented domains and one Bloch domain wall (Fig. 4(a)). These subunits are rotated within the surface plane; Fig. 4(b,c) shows an example of such a maze structure and division of magnetic domains into small units assuming a parallel alignment of the magnetic domains within one sub-unit. L_x represents the correlation length of one ordered subsystem parallel to the domain wall (Fig. 4(c)). The total scattering cross section can be written as sum over the scattering from all possible sub-units. The process is described in more detail by Stellhorn [10]. For the high-PMA FePd layer used here, MFM measurements show a maze distribution of magnetic domains with an average direction θ_{av} tilted away from the incident neutron beam direction of about 20°, and with a distribution of domain directions around the mean

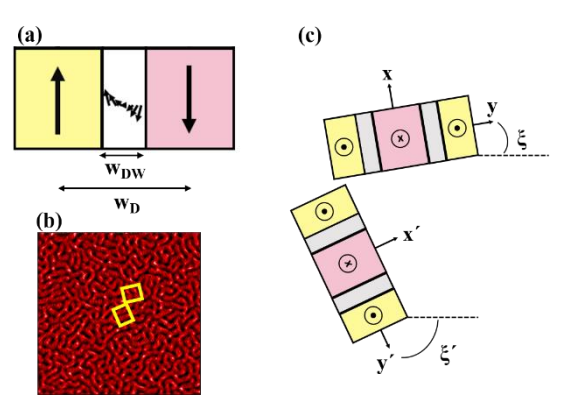


Fig. 4. (a) Side-view of one subunit with two out-of-plane oriented domains of size w_D and one Bloch domain wall of size w_D w. (b) 3x3 μm MFM measurement on high-PMA FePd with a maze domain structure – the yellow boxes denote two subunits. (c) In-plane rotation of pairs of subunits about different angles ζ. The correlation length parallel to the domain wall is given by L_x .

direction which can be roughly approximated with a Gaussian-type shape (Fig. 5). This distribution is used in our model. The reasons for the preferential in-plane domain orientation are not germane to this article, but are discussed elsewhere [10,11].

Within this model, the incident and outgoing polarization vectors \vec{P}_i and \vec{P}_f are included via the density matrices of the incident and reflected neutron beam $\hat{\rho}_i = \frac{1}{2} (\hat{1} + \vec{P}_i \vec{\hat{\sigma}})$ and $\hat{\rho}_f = \frac{1}{2} (\hat{1} + \vec{P}_f \vec{\hat{\sigma}})$ using:

$$\frac{d\sigma}{d\Omega}(\theta_i, \theta_f, \overrightarrow{Q}_{//}) = tr(\hat{\rho}_f \hat{F}_{fi} \hat{\rho}_i \hat{F}_{fi}^{\dagger})$$
(10)

where $\hat{F}_{fi} = \hat{F}_{fi}(\overrightarrow{Q}_{//})$ is the scattering amplitude operator (in the space of spin states) and \hat{F}_{fi}^{\dagger} its Hermitian conjugate.

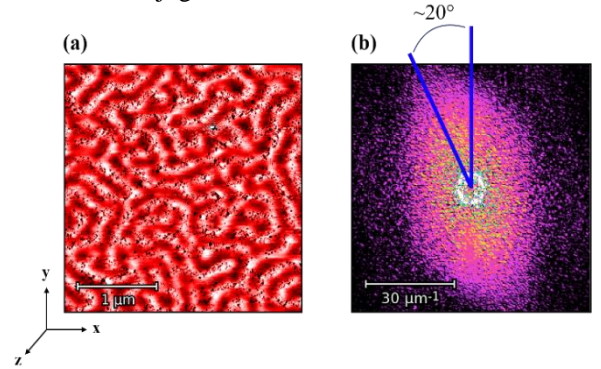


Fig. 5. (a) 3x3 μm MFM measurement on the high-PMA FePd sample measured by GISANS. A maze domain structure is seen. (b) The Fourier transform of panel (a), showing a nearly Gaussian-type domain distribution around a mean angle tilted 20° from the incident neutron beam direction.

3 Neutron spin adiabaticity

3.1 Magnetic field measurements & simulations using COMSOL

In this section we discuss how the polarization direction may have been affected by adiabaticity during spintransport along the beam path: The setup at vSANS, NIST [17] is illustrated in Fig. 6. The neutron beam went from right to left. The incoming neutrons' polarization in the guide field was oriented in the y-direction, then rotated into the z-direction (axis parallel to the surface normal) at the sample position by the magnetic field applied from the pole-pieces of the Titan electromagnet, and was again rotated in the x-direction for the ${}^{3}\text{He-cell}$ analyzer. Two guide fields just in front of and behind the pole-pieces (not shown in Fig. 6, positions marked in Fig. 7) kept the magnetic field along y and rotated it to the x-direction, respectively. A precise measurement of the 3D magnetic field configuration along the beam path has been carried out using a 3D Hall probe. The results are compared with simulations of the magnetic field configuration using finite element computational software COMSOL Multiphysics [23].

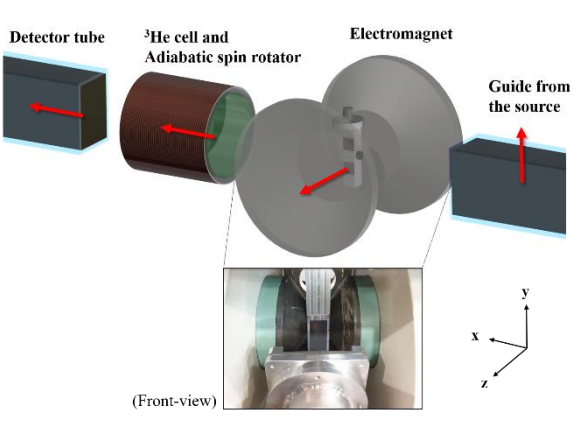


Fig. 6. (a) Beamline setup and polarization direction (red arrows) of the polarized GISANS experiments at vSANS, NIST [18], using an electromagnet with pole pieces extending close to the cryoshield containing the sample holder, visible in the inset on the bottom.

The neutron adiabaticity along the beam path may be calculated if the magnetic field configuration of the whole beamline setup is known. This can be simulated using COMSOL Multiphysics. Individual beamline components are included with their basic physical properties (such as the dielectric constant or magnetic permeability). Sources of magnetic field are included either as permanent magnets or current-carrying coils as relevant. The 3D magnetic field distribution ($(B_{xy}B_{yy}B_z)$ in Tesla) is then calculated in a predefined area as a function of the position (x,y,z) along the neutron flight path.

Care needs to be taken when defining the mesh (shape, size, density, and number of elements within the geometry) on which the interpolation and accuracy of the solution is based on: a fine mesh that scales with the size of the object is imposed on the focused regions and the magnetic components, moderate mesh size in regions connecting them, and coarse meshing can be used everywhere else. Our input model is shown in Fig. 7. This yields a magnetic field configuration \vec{B}_{COMSOL} and adiabaticity A_{COMSOL} as given in Fig. 8.

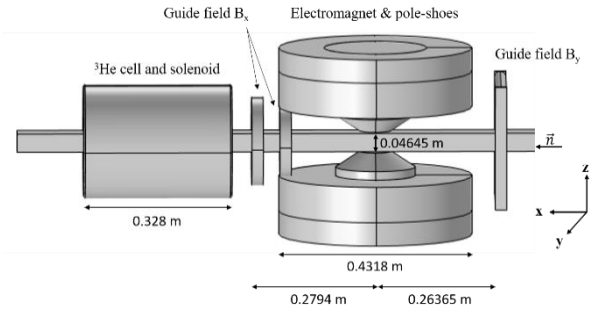


Fig. 7. The input model to COMSOL of the components of the vSANS beamline at NIST [18] used for the polarized GISANS measurements discussed here.

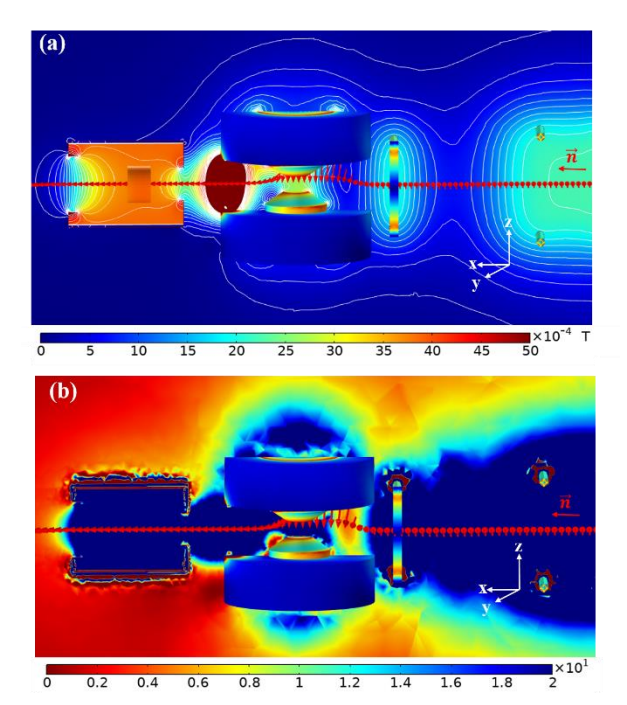


Fig. 8. (a) The calculated magnetic field map of the polarized GISANS setup at vSANS, NIST. The colour scale denotes the strength of magnetic field $B = |(B_x, B_y, B_z)|$ in (10^{-4} T) . The red arrows denote the magnetic field direction along the neutron beam path. The neutrons are incident from the right moving left, as in Figures 6 and 7. Two guide fields in front of and behind the sample have been installed to adiabatically rotate the neutron spin. (b) The calculated adiabaticity map. There is a region just before the sample with a critically low adiabaticity value. The magnetic field vector along the neutron beam path is again shown by red arrows denoting the magnetic field vector.

These computational results were then compared with magnetic field measurements of the actual setup used at vSANS (NIST), made using a 3D Hall probe mounted on a fixed stage which could be slid through the setup, along the neutron beam path. The resulting measured field, $(B_x, B_y, B_z)_{meas}(x)$ is compared with $\overrightarrow{B}_{COMSOL}$ and A_{COMSOL} in Fig. 9.

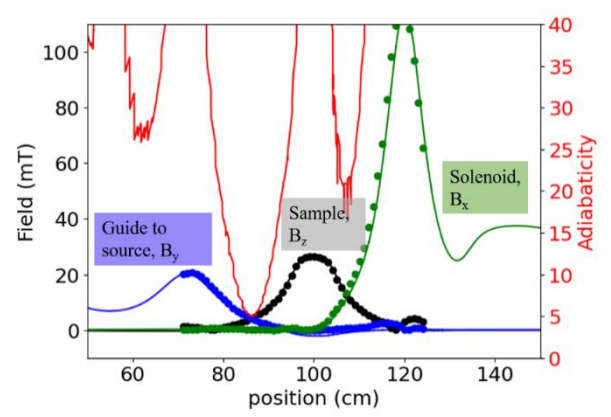


Fig. 9. The measured (circles) and simulated (lines) magnetic field components (B_x, B_y, B_z) (left axis) and the calculated adiabaticity (right axis) as a function of the position x (measured as the distance from the opening of the source guide) along the neutron flight path. The labelled guide fields are as shown in Fig. 6.

From this, two conclusions can be drawn: (i) a critically low adiabaticity A < 5 is reached just in front of the electromagnet during the rotation of polarization

from the y to the z-direction, indicating a possible misalignment of \vec{P} with respect to \vec{B} , and (ii) the measured and simulated field strengths coincide and so \vec{B}_{COMSOL} can be used as an input to the neutron ray-tracing program McStas 2.7 [24,25].

3.2 Neutron polarization simulations using McStas

McStas is a neutron ray-tracing Monte-Carlo simulation package [24,25]. It simulates the parameters of an ensemble of neutrons (the intensity, position, velocity, and polarization) starting from a source and passing through defined beamline components. Here, we concentrate on how the neutron beam polarization \vec{P}_{McStas} changes as the neutrons travel through the magnetic field map calculated using the COMSOL simulations described and validated above. The most relevant parameters defining the neutron polarization are the step-size of the magnetic field imported from the COMSOL simulations, the angular accuracy (the threshold below which two magnetic fields are considered to be parallel), the neutron wavelength and distribution, and the incident polarization after the polarizer. The resulting neutron polarization $\vec{P}_{McStas,sample}$ at the sample position of the neutrons passing through \vec{B}_{COMSOL} is then compared with the applied field direction $\vec{B}_{COMSOL,sample}$ at the sample position via the angle α , defined as

$$\alpha = \cos^{-1} \left(\frac{\vec{B}_{COMSOL,sample} \cdot \vec{P}_{McStas,sample}}{|\vec{B}_{COMSOL,sample}|| \vec{P}_{McStas,sample}|} \right)$$
(11)

The neutron polarization in out-of-plane direction (along the applied magnetic field) and the angle α between $\vec{P}_{\text{McStas,sample}}$ and $\vec{B}_{COMSOL,sample}$ as function of the transversal positions y and z around the sample position are depicted together with the sketched position and size of the investigated FePd thin film in Fig. 10. Table 2 lists

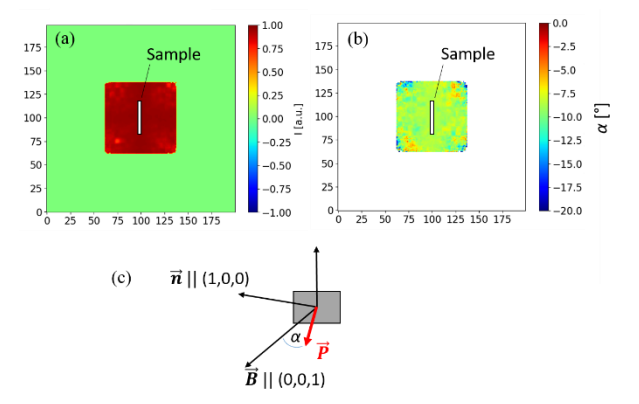


Fig. 10. The results of the McStas simulation: (a) the degree of polarization in the out-of-plane direction (along the applied magnetic field direction), and (b) the angle α between the $\vec{P}_{McStas,sample}$ and $\vec{B}_{COMSOL,sample}$. (c) A sketch of the sample geometry showing the incident neutron beam direction (x), the magnetic field vector along the surface normal (z), and the tilted polarization \vec{P} .

the relevant parameters resulting from the McStas simulations.

Table 2. Parameters and results from the McStas simulation

Step size of magnetic field	2.5 mm
Angular accuracy	1°
Wavelength + distribution	$\lambda = 8 \text{ Å}, \Delta \lambda = 0.96$
Initial polarization	$\vec{P}_{McStas,in} = (0, 0.97, 0)$
Resulting polarization at the sample position	$\vec{P}_{McStas,sample} = (0.015, -0.077, -0.966)$
Magnetic field vector at the sample position	$\vec{\mathbf{B}}_{COMSOL,sample} = (0.1, -0.2, 2.7) \text{ (mT)}$
Angle α between $\vec{P}_{McStas,sample}$ and $\vec{B}_{COMSOL,sample}$	<i>α</i> = 9°

The simulation yields an angle of $\alpha = 9^{\circ}$ between the neutron polarization and the magnetic field direction. This result can then be included in the simulations of the magnetic scattering pattern of polarized GISANS measurements described in Section 2.3 by including the value of $\vec{P}_{McStas, sample}$. Depolarization of the neutron beam due to stray fields from the sample can lead to an additional rotation of \vec{P} . We note that the electromagnet, which includes the sample stage, was tilted 4.7° away from the horizontal; this was included in the COMSOL simulations. Hence, the given $\vec{B}_{COMSOL,sample}$ includes this tilt of the applied field at the electromagnet w.r.t to the z-direction. As the sample stage is connected to the electromagnet, the magnetic field orientation with respect to the sample was unchanged by this tilt and did not contribute to the angle between neutron polarization and the sample normal.

The strong agreement between the measured and simulated magnetic fields gives confidence in the simulated adiabaticity shown in Fig. 9. Critically low values of A for the neutron beam are reached in front of the sample position. As is clear from Eq. 5, this can have an effect on the resulting magnetic scattering pattern, as it means that scattering from the chiral magnetic moments with $\widetilde{M}_{\perp} \times \overline{M}_{\perp}$ could become visible as the asymmetry measured $I(Q_y, Q_z)$ in Fig. 2.Further improvements of the presented simulations and resulting polarization directions are still being performed, including comparisons with the neutron ray tracing software VITESS, and checking finer angular accuracies for the McStas simulation. However, the presented results show the necessity of a detailed investigation of the neutron beam adiabaticity and polarization throughout the beamline, to aid in constraining the simulation parameters required for calculations of the scattering cross section, particularly complex magnetic models.

4 Conclusions

Our results show that neutron polarization simulations are an integral part of experiments relying on polarized neutrons. They highlight that significant neutron polarization misalignments may occur even when the magnetic field direction at the sample point and the neutron polarization measurements look promising. The detailed simulations help constrain calculations of the cross section that start from the sample properties by providing detailed inputs for the neutron polarization and the magnetic field. They also provide aspect for a comprehensive data analysis of magnetic scattering cross sections, especially given that the magnetic field direction at the point of sample scattering and the neutron polarization may look good even while significant neutron polarization misalignment is occurring. Benefits are the minimization of unknown simulation parameters and a global understanding of the influence of the magnetic field vector as a function of the neutron beam path. Especially guide field conditions, with the constraint of low field values at the sample position, and a non-adiabatic neutron transport imply the need of precise scattering cross section simulations. If concurrently at the same time, complex magnetization distributions within the investigated samples have to be considered, the need of minimizing unknown parameters is even stronger.

We present a reduction of unknown parameters for the simulation of scattering cross sections from polarized GISANS measurements with polarization analysis. We have performed a comprehensive investigation of the neutron polarization orientation with respect to the applied magnetic field vector using magnetic field modelling in COMSOL and neutron ray tracing in McStas, and a comparison with magnetic field vectors obtained from measurements along the neutron beam path of the employed polarized GISANS setup. As a result, a deviation from the direction of polarization with respect to the applied magnetic field direction has been quantified, opening the possibility to be considered in simulations of the scattering cross section of the investigated sample based on the Distorted-Wave-Born-Approximation.

Acknowledgements

This research is funded in part by the Tillväxtverket grant. We acknowledge the support of the National Institute of Standards and Technology, U.S. Department of Commerce, in providing the neutron research facilities used in this work, and thank for the kind help during the measurements. Additionally, we acknowledge following support:

- 1. Discussions on the neutron polarization and adiabaticity at vSANS, NIST, with Julie Borchers
- 2. Support for the measurements and their analysis of polarized GISANS by Thomas Brückel & the JCNS The identification of any commercial product or trade name does not imply endorsement or recommendation by the National Institute of Standards and Technology.

References

- 1. A. Wiedenmann, Physica B **356**, 246–253 (2005).,
- F. Tasset, P. J. Brown, J. B. Forsyth, J. Appl. Phys. 63, 3606-3608 (1988).
- 3. M. Janoschek, S. Klimko, R. Gähler, B. Roessli, P. Böni, Phys. B: Condens. Matter **397**, 125-130 (2007).
- M. T. Rekveldt, Nucl. Instrum. Methods Phys. Res. B 114, 366-370 (1996).
- B. Toperverg, Phys. Met. Metallogr. 116, 1337-1375 (2015)
- 6. E. Kentzinger, U. Rücker, B. Toperverg, F. Ott, T. Brückel, Phys. Rev. B 77, 104435 (2008)
- 7. D. Korolkov, P. Busch, L. Willner, E. Kentzinger, U. Rücker, A. Paul, H. Frielinghaus, T. Brückel, J. Appl. Crystallogr. **45**, 245-254 (2012)
- 8. D. E. Laughlin, K. Srinivasan, M. Tanase, and L. Wang, Scr. Mater. **53**, 383-388 (2005)
- 9. J. M. D. Coey, Magnetism and Magnetic Materials, Cambridge University Press (2010)
- A. Stellhorn, PhD Thesis "Interplay of proximity effects in superconductor/ferromagnet heterostructures, RWTH Aachen University (2021)
- A. Stellhorn, A. Sarkar, E. Kentzinger, M. Waschk, P. Schöffmann, S. Schröder, G. Abuladze, Z. Fu, V. Pipich, T. Brückel, J. Magn. Magn. Mater. 476, 483-486 (2019).
- 12. A. Hubert and R. Schäfer, "Magnetic Domains", Springer-Verlag GmbH (2008)
- G. van der Laan, K. Chesnel, M. Belakhovsky, A. Marty, F. Livet, S. Collins, E. Dudzik, A. Haznar, J. Attané, Superlattices Microstruct. 34, 107-126 (2003)
- D. Ravelosona, A. Cebollada, F. Briones, C. Diaz-Paniagua, M. A. Hidalgo, F. Batallan, Phys. Rev. B 59, 4322-4326 (1999)
- A. Fert, V. Cros, J. Sampaio, Nat. Nanotechnol. 8, 152-156 (2013)
- S. D. Pollard, J. A. Garlow, K.-W. Kim, S. Cheng, K. Cai, Y. Zhu, H. Yang, Phys. Rev. Lett. 125, 227203 (2020)
- C. Fermon, F. Ott, B. Gilles, A. Marty, A. Menelle, Y. Samson, G. Lego, G. Francinet, Phys. B 267-268, 162-167 (1999)
- W. Chen, K. L. Krycka, S. M. Watson, J. G. Barker, J. Gaudet, H. Burral, J. A. Borchers, J. Phys. Conf. Ser. **2481**, 012006 (2023)
- J.G. Barker J.J. Moyer, S.R. Kline, G.V. Jensen, J.C. Cook, C. Gagnon, E.G. Kellym J.P. Ghabot, N.C. Maliszewskyj, C. Parikh, W.C. Chen, C.J. Glinka, J. Appl. Crystallogr. 55, 271-283 (2022)
- 20. M. Blume, Phys. Rev. 130, 1670 (1963)
- 21. F. Tasset, P. J. Brown, E. Lelièvre-Berna, T. Roberts, S. Pujol, J. Allibon, E. Bougeat-Lami, Physica B **267-268**, 69-74 (1999)

- 22. W. Schweika, J. Phys. Conf. Ser. **211**, 012026 (2010)
- COMSOL Multiphysics® v. 6.1. www.comsol.com. COMSOL AB, Stockholm, Sweden
- 24. P. Willendrup, K. Lefmann, J. Neutron Res. **22**, 1-16 (2020)
- 25. P. Willendrup, K. Lefmann, J. Neutron Res. **23**, 7-27 (2021)